RESEARCH PAPER

A Facile Synthesis and Characterization of Surfactant (CTAB/TSC/TX-100) Assisted Ir-Sn Bimetallic Nanoparticles

Anjali Goel, Sudha Tomar *, and Shikha Tomar

Department of Chemistry, KGC, Gurukul Kangri University, Haridwar, Uttrakhand, 249407, India

ARTICLE INFO

ABSTRACT

The present work is mainly focused on the synthesis and characterization of surfactant-assisted Ir-Sn BMNP (bimetallic nanoparticles) using modified polyol method. CTAB (Cetyltrimethylammonium bromide), TSC (Trisodium citrate), and TX-100 (Triton X-100) as cationic, anionic, and nonionic surfactant respectively are used to study their effect on the particle size, morphology and their stability. The synthesized particles are characterized by XRD, FE-SEM, EDAX, elemental mapping, TEM, HR-TEM, XPS and FT-IR, TGA, DTG, and DTA techniques. UV-Vis spectroscopy is used to monitor the synthesis of nanoparticles. The XRD patterns of all samples confirm that Ir-Sn BMNP are amorphous in nature. The influence of surfactant on the morphology and particle size of Ir-Sn BMNP samples was examined by the FE-SEM technique. The FE-SEM figures demonstrate that the particles of bimetal are in nano size, highly dispersed, and pseudo spherical in shape with smooth surfaces. The approximate crystallite (particle/grain) size of CTAB, TSC, and TX-100 assisted samples are ~1.39 nm (39 nm), ~2.2 nm (59 nm), and ~5.79 nm (89 nm) respectively, which are estimated from TEM and FE-SEM images. The presence and distribution of Ir and Sn elements in the BMNP is determined through EDAX and elemental mapping respectively. These techniques show that CTAB assisted Ir-Sn BMNP sample is in alloy form but TSC and TX-100 samples are in core-shell form, where the Ir core is surrounded by Sn shell. The XPS confirms the metallic state (Ir0), and the dual valence state of Sn (Sn^{2+} and Sn^{4+}) is in the Sn 3d core level.
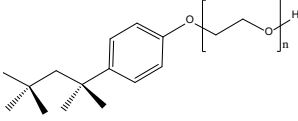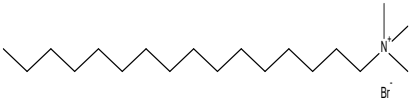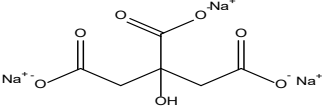
INTRODUCTION

Bimetallic nanoparticles are widely used in various fields such as medicine [1-3], optical [4], electrochemical [5-7], and catalyst [8]. In the area of the catalyst, the bimetallic nanoparticles used as oxidation, reduction or oxidation degradation of chemicals e.g., dyes [9-11], glucose [12], carbon monoxide [13], benzyl alcohol [14], methanol [15], and toluene [16], the dehydrogenation of propane [17] and hydrogenation of nitroarene [18]. In the bimetallic catalysts, the electronic effect plays an important role that describes the charge transfer. Bimetallic nanoparticles have a larger surface area that increases their adsorption. Therefore these acts as efficient catalyst comparably to the monometallic nanoparticles [19]. In the various application fields, bimetallic catalysts have been used due to the cause of multifunctional nanomaterials. The reason behind the behavior of multifunctional is the ''synergistic effect,'' which exists amid the two metals [20]. Tin (Sn) base bimetallic nanoparticles systems such as

* Corresponding Author Email: sudhatomar008@gmail.com

Table 1. Details of the surfactants used.

IUPAC name	Formula	Molar mass (g mol^{-1})	Structure
Polyoxyethyleneoctyl phenyl ether (TX-100)	$C_{14}H_{22}O(C_2H_4O)_n)$	647	
Hexadecyl-trimethyl-ammonium bromide (CTAB)	$(C_{16}H_{33})N(CH_3)_3Br$	364.45	
Trisodium 2-hydroxypropane-1,2,3,-tricarboxylate (TSC)	$Na_3C_6H_5O_7$	258.06	

Ni-Sn [21], Pt-Sn [22], Pd-Sn [23], Bi-Sn [24, 25], Ru-Sn [26], and Rh-Sn [27] have been observed as excellent catalyst behavior because of the wide band gap energy of Sn [28, 29]. Noble metal Iridium (Ir) nanostructures have gained significant research interest due to their unique catalytic, optical, and electronic properties for promising applications, which significantly depend on their size, shape/morphology, and composition [30-32]. At the nanoscale, the noble metal Iridium (Ir) reveals interesting catalytic, electronic, optical, mechanical, and magnetic properties like novel silver, gold, and platinum metals [33, 34], which have been extensively studied. The noble metal Iridium (Ir) also possesses superior stability, catalytic activity and corrosion resistance due to the unique electronic structure and large surface area to volume ratios as same as platinum group metal like ruthenium, rhodium, palladium, osmium, and platinum [35-38]. The wide study has already been done on the iridium bimetallic nanoparticles systems like Ir-Ni [39], Ir-Ru [40, 41], Ir-V [42], and Pt-Ir [43]. Courtais et al. 2014 studied iridium based bimetallic alloys, and they observed that the iridium based bimetallic alloys catalyst can be used for direct ethanol fuel cells [44]. Xu et al. 2020 has studied the Controllable synthesis of Ir(Rh)-Sn/SiO$_2$ bimetallic catalysts and they used the Controllable synthesis of Ir(Rh)-Sn/SiO$_2$ bimetallic as a catalyst in the production of ethanol from hydrogenolysis of ethyl acetate [45].

Nowadays, the surfactants are in trend to control the properties like shape, size, surface-to-volume ratio, and quantum confinement effects of the nanoparticles. In the nanoparticles, high specific surface area and narrow pore size can be achieved by the addition of a surfactant [46]. In the synthesis of the nanoparticles, various type of surfactant plays an important role, which control the shape of nanoparticles [47]. Yu-de Wang et al. has analyzed the effect of the CTAB surfactant on the SnO$_2$ system, and they observed that the SnO$_2$ nanoparticles were highly crystalline and largely mono disperse oxide in the range of 15 to 25 nm [48]. Habulat et al. 2020 proposed the study of (TX-100) assisted SnO$_2$ nanoparticles via hydrothermal method to use the degradation of organic textile dye [49].

From the literature survey, it has been observed that the surfactant-assisted nanoparticles are very useful in various fields due to the shape, size, surface-to-volume ratio, and quantum confinement effects. So we are very interesting to see the effect of the addition of Cationic (CTAB), anionic (TSC), and nonionic (TX-100) surfactants in the Ir-Sn metal. In the last recent years, no reports have been found on the Ir-Sn bimetallic nanoparticles with variously charged surfactants. In the present work, the surfactant-assisted Ir-Sn bimetallic nanoparticles have been formed via modified polyol method using Iridium trichloride (IrCl$_3$.xH$_2$O), tin chloride (SnCl$_2$.2H$_2$O) (precursor salt). The organic surfactant CTAB (cationic), TSC (anionic), and TX-100 (nonionic) have been used as a stabilizer in this process (see Table 1). To analysis, the effect of surfactants on the Ir-Sn bimetallic nanoparticles, various kinds of characterization techniques such as XRD, FE-SEM, EDAX, elemental
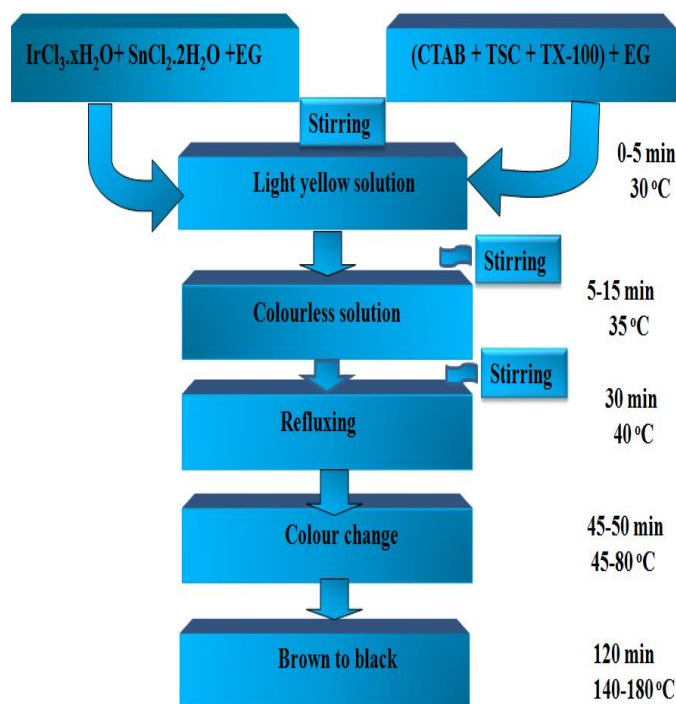
Fig.1. The flow chart of the synthesis of surfactant assisted Ir-Sn bimetallic nanoparticles.

mapping, TEM, HR-TEM, XPS, FT-IR, TGA, DTG, and DTA have been employed. These techniques provided the wide details of surfactant-assisted Ir-Sn bimetallic nanoparticles.

MATERIALS AND METHODS

All reagents are of analytical grade and used without further purification. Iridium trichloride (IrCl$_3$.xH$_2$O), tin chloride (SnCl$_2$.2H$_2$O) (precursor salts) and ethylene glycol (solvent and reducing agent) were purchased from Sisco Research Laboratory, Mumbai. Sodium hydroxide pellets were obtained from Merck. Cationic (CTAB), anionic (TSC) and nonionic (TX-100) surfactants purchased from Thomas Baker were used as a stabilizing agent. All solutions were prepared in double-distilled water.

Preparation of nanoparticles

In the present work, the surfactant assisted Ir-Sn BMNP samples with molar ratios 2:1 using precursor salts of iridium chloride (IrCl$_3$.xH$_2$O) and tin chloride (SnCl$_2$.2H$_2$O) were synthesized using modified polyol reduction method [50]. Precursor salts of iridium tri chloride and tin chloride in 2:1 molar ratios were dissolved in 25 ml ethylene glycol. Stabilizers act as capping agents, which

provide a coating around the particles, this satisfy the high energy of particles and skip them from agglomeration. CTAB, TSC and TX-100 are the most common and frequently used stabilizers. The pH of solution was alter by addition of 1 ml NaOH added slowly into the reaction mixture [51]. After being stirred at room temperature, the entire solution was refluxed for 2 h in oil bath at 140-180 °C temperature. After refluxing, the color of the solution becomes blackish brown from pale yellow. The flowchart of the method is demonstrated through Fig. 1. The reaction progress has been monitored by UV-Vis spectroscopy. The appearance of new band in the spectrum shows the formation of new species due to reduction of precursor salt. The Fig. 2 shows UV- Visible spectra of surfactant (CTAB, TSC, TX-100) assisted Ir-Sn bimetallic nanoparticles. The spectrums of UV-Vis spectroscopy reveal a peak around 352 nm which was initially at 280 and 232 due to IrCl$_3$ and SnCl$_2$ respectively. These peaks verify the formation of bimetallic nanoparticles [52, 53].

Mechanism involve in formation of Iridium tin bimetallic nanoparticles:

The proposed mechanism, which has been used to prepare the surfactant-assisted iridium
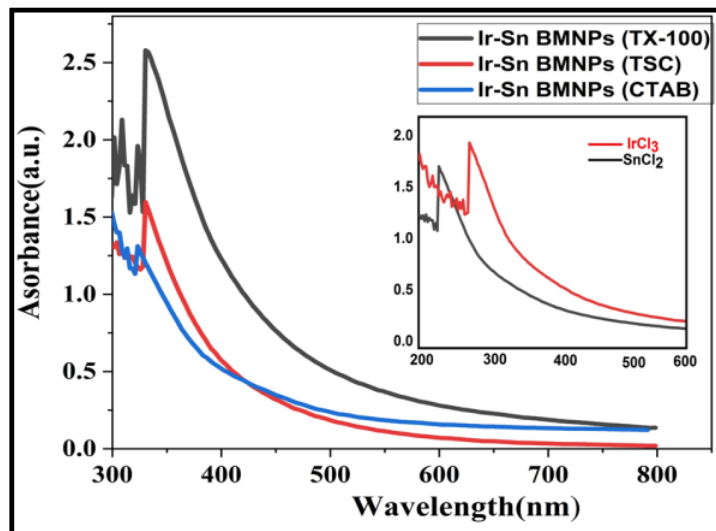
Fig. 2. UV- Visible spectra of surfactant (CTAB, TSC, TX-100) assisted Ir-Sn bimetallic nanoparticles and precursor salts.
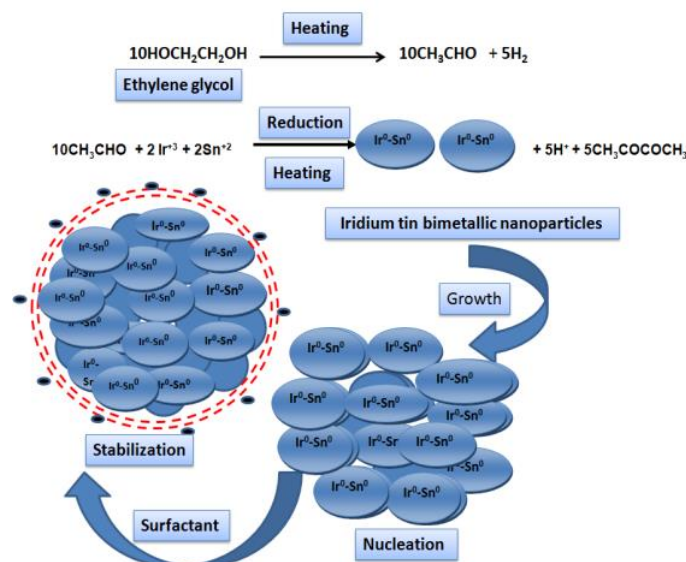

Fig. 3. Mechanism of formation of surfactant assisted Ir-Sn bimetallic nanoparticles.

tin bimetallic nanoparticles are known as a general reduction process, is shown in Fig. 3. In this mechanism, ethylene glycol is used as both solvent and reducing agent, which converts into acetaldehyde through the oxidation process. At the onset, the complex is made between acetaldehyde (CH_3CHO) and ions present in the solution (Ir^{+3}, Sn^{+2}), which reduces Ir and Sn ions into the Ir^0-Sn^0 seeds, which grow through nucleation and result into bimetallic nanoparticles. The surfactant like CTAB, TSC, and TX-100 prevents the agglomeration and stabilities the Ir-Sn bimetallic nanoparticles.

Equipments

The micro structural analysis of bimetallic nanoparticles was determined from X-ray diffraction (XRD) (Panalytical's X'Pert Pro, under Cu-Kα radiation, with 2 theta ranging 20° - 80°) average Crystallite size of the samples were determined using the Debye Scherrer equation, Field emission-scanning electron microscopy (FE-SEM) (Hitachi (H-7500) and elemental composition
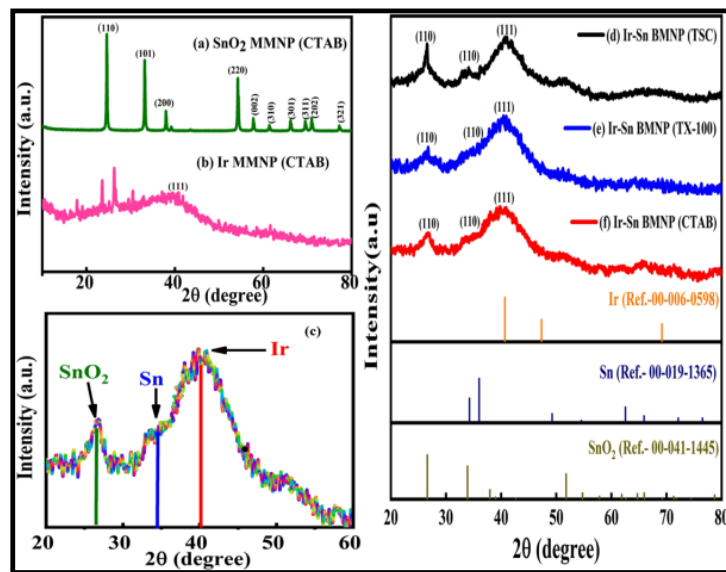
Fig.4. The XRD pattern of surfactant assisted Ir and SnO$_2$ MMNP, Ir-Sn BMNP samples, (a) Sn MMNP (CTAB), (b) Ir MMNP (CTAB), (d) Ir-Sn BMNP (TSC), (e) Ir-Sn BMNP (TX-100), and (f) Ir-Sn BMNP (CTAB), (c) The inset represents the main peak area, is showing the presence of Ir, Sn and SnO$_2$ in the surfactant (CTAB, TSC, and TX-100) assisted BMNP samples.

were investigated by using EDAX and elemental mapping respectively. TEM (transmission electron microscope) Characterization, for the BMNP Crystallite size distribution was performed using (Hitachi (H- 7500). High resolution transmission electron microscope (HR-TEM) were performed using (HRTEM 200kv JEM 2100 Plus), operate at an accelerating voltage of 20-200kv. Samples for HR-TEM analysis were obtained by using dilute solution of nanocrystals. The double beam UV-Vis absorption spectroscopy (Systronic-2203 spectrophotometer), was used to study the progress of the nanoparticles formation. The oxidation state and chemical composition of CTAB assisted Ir-Sn BMNP sample were investigated using X-ray photoelectron spectroscopy (XPS PHI 5000 versa probe III). The Fourier transform infrared (FT-IR) spectra were measured with FTIR (Perkin Elemer) in the range of 4000-400 cm^{-1} using the KBr Pellet technique. The thermal analysis (TGA, DTG and DTA) of the samples were investigated using a SII 6300 EXSTAR , at a constant heating rate of 10 ^{o}C/min over a temperature range of 35-1000 ^{o}C using alumina powder (10 mg) as a reference material.

RESULTS AND DISCUSSION
X-ray diffraction (XRD) analysis

The X-ray diffraction technique has been employed to examine the crystal structure and crystallinity of surfactant assisted Ir, Sn nanoparticles. The XRD pattern of Ir MMNP (CTAB), SnO$_2$ MMNP (CTAB) and Ir-Sn surfactant assisted BMNP samples are demonstrated in Fig. 4. In Fig. 4 (a), four distinctive peaks of CTAB assisted SnO$_2$ MMNP sample have been observed at 26.5°, 33.8°, 37.9°, 54.7°, 57.7°, 61.5°, 66.2°, 69.5°, 71.3°, and 77.4° with miller indices (hkl) value (110), (101), (200), (220), (002), (310), (301), (311), (202), and (321) respectively. The data of this sample is exactly matched with the JCPDS (card no. 00-041-1445), which indicates the formation of tetragonal rutile-like SnO$_2$ MMNP sample. Also in Fig. 4 (b), only one peak of the CTAB assisted Ir MMNP sample has been observed at 41.1° with (hkl) value (111) plane, which matched with (card no.00-006-0598). Fig. 4 (d, e, and f) the XRD data of Ir-Sn surfactant assisted BMNP (CTAB, TSC, TX-100) samples have been demonstrated with JCPDS card no.(00-041-1445 (for SnO2), 00-019-1365 (for Sn), and 00-006-0598 (for Ir)), those are confirmed the Ir is presented in metallic state and Sn is present in metallic and tin oxide form. Broad peaks at about 40.8° with (hkl) value (111), peak at 34.15 with (hkl) value (110), and the peak at 25° with (hkl) value (110) corresponds to Ir(0), Sn(0), and SnO$_2$ respectively. These peaks represent the amorphous nature of the bimetallic nanoparticles. The comparison of the data between SnO$_2$ and Ir MMNP, and Ir-Sn surfactant (CTAB) assisted-

Table 2. Calculated a Crystallite size of mono and bimetallic nanoparticles

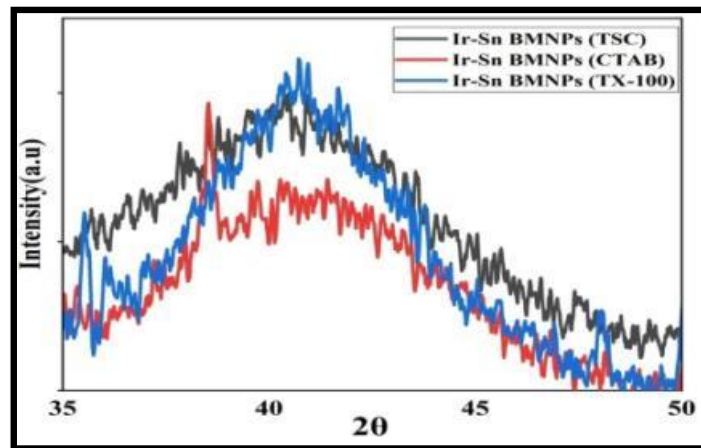| Sample	Ir MMNP (CTAB)	SnO$_2$ MMNP (CTAB)	Ir-Sn BMNP (CTAB)	Ir-Sn BMNP (TSC)	Ir-Sn BMNP (TX-100)
Crystallite size (nm)	1.2 nm	40 nm	0.19 nm	1.2 nm	1.3 nm

Fig.5. Primary peak of surfactant (CTAB, TX-100 AND TSC) assisted Ir-Sn BMNP samples.

BMNP samples show shifting in 2 theta value from 41.1° to 40.8° and 26.5° to 25° due to some interaction among iridium (Ir) and tin (Sn). The Fig.4 (c) demonstrated the broad peaks of Ir-Sn surfactant (CTAB, TSC, and TX-100) assisted BMNP samples, and all broad peaks reveals presence of some amount of Ir-Sn alloy along with SnO$_2$ in the structure of Ir-Sn BMNP samples, which confirm the formation of bimetallic nanoparticles with FCC lattice. Approximate crystallite size (D) of all the samples has been evaluated by employing Debye-Scherer equation-

$$D = \frac{k\lambda}{\beta COS\theta}$$

Where, *k* = pre factor, λ= wavelength of the incident beam (CuKα), and β = FWHM of Peak.

The calculated values of crystal sizes are shown in the Table 2. The presented data show that Ir-Sn BMNP have small crystallite size as compared to monometallic nanoparticles. This may be because of small ionic radii of Ir as compared to Sn. On the other hand, the value of crystallite size of Ir-Sn BMNP sample with all the above stated surfactants is also determined and it has been found that Ir-Sn BMNP sample with CTAB surfactant has the lower crystallite size as compared to TSC and TX-100 samples, which may be due to an increment

in the imperfection of crystal structure [54]. In Fig. 5, the CTAB assisted sample, which has the smallest crystalline size revealed a low-intensity peak compared to TSC and TX-100 assisted samples [55]. This corroborates that the surfactant restricts the growth of particles in the samples and play an important role in preventing the rapid flocculation and aggregation of the particles [56]. Surfactants cap (or passivate) the surface of nanoparticals and exert a strong influence on its morphology by controlling the growth rate of various crystallographic surfaces and generating orientations in crystal formation. This means that the growth of nanoparticles is controlled by the diffusion and attachment rates of surfactants onto the nanoparticle surface [57].

Field Emission Scanning Electron Microscope (FE-SEM) analysis

The surface morphology and approximate particle/ grain size of the surfactant-assisted Ir-Sn BMNP samples have been estimated through the FE-SEM technique. The FE-SEM images are shown in Fig. 6, clearly bring out the variation in the particle size as change the surfactant CTAB (Cationic), TSC (Anionic), and TX-100 (Nonionic) adequately, and also observed that the all synthesized surfactant-assisted Ir-Sn BMNP have an approximately pseudo
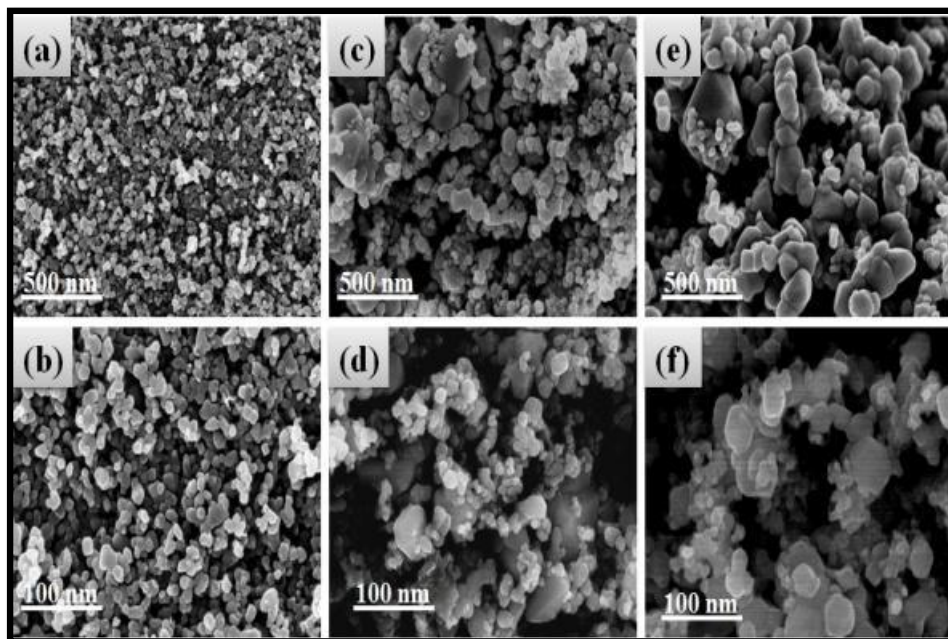
Fig. 6. FE-SEM Images of surfactant assisted Ir-Sn BMNP samples (a, b) Ir-Sn BMNP (CTAB), (c, d) Ir-Sn BMNP (TSC) and (e, f) Ir-Sn BMNP (TX-100).

spherical shape. The particle size of all samples has been evaluated using Image J software [58, 59], and it is observed that the average size of particle/ grain change ~39 nm, ~59 nm, and ~89 nm with adding surfactant CTAB (Cationic), TSC (Anionic), and TX-100 (Nonionic) respectively. From the FE-SEM images, it has been found that the morphology of CTAB (Cationic) Ir-Sn BMNP sample is dense with a smooth surface and uniform size particle compared to TSC, and TX-100 assisted Ir-Sn BMNP samples. But on the other hand, the TSC, and TX-100 assisted Ir-Sn BMNP samples in having the porous morphology with non-uniform particle size. In another way CTAB can form a shell surrounding the particles to prevent them from aggregating to larger particles and grain growth as a result of its Steric effect and mono-dispersed Ir-Sn BMNP may be obtained finally [60]. The small particle size and less agglomeration play the crucial role of CTAB surfactant in controlling the nucleation and crystal orientation [54]. Hence, from the above findings, the synthesis of Ir-Sn BMNP nanoparticles via simple polyol method using CTAB surfactant is very usable. The influence of the presence of the surfactant during the growth of nanoparticles, not just induces the nanoparticles to feature the highly active surface of the lattice, but also stimulates the nanoparticles

to have the portent of the large surface area, ordered structure, and abundant pores. These types of alterations mend the physicochemical properties of the nanoparticles, due to which the performance of the nanoparticles is increased [61].

Energy-dispersive X-ray spectroscopy (EDAX) and Elemental mapping analysis

The atomic composition of the Ir-Sn surfactant assisted BMNP samples are estimated using the EDAX technique. The EDAX spectrum and elemental composition of Ir-Sn surfactant assisted BMNP samples are shown in Fig. 7, which confirms the presence of Ir, Sn, C and O elements in required samples, and verify the purity and atomic composition of synthesized BMNP samples. Some additional peaks are also observed in the EDAX spectrum, which may be related to the Au (gold) metal because Au is used for coating over the sample during prepare for FE-SEM characterization. The elemental mapping of surfactant assisted Ir-Sn BMNP samples are shown in Fig. 8. The Ir and Sn elements are represented via red and green color, respectively. The existence of Ir, Sn elements in the surfactant assisted Ir-Sn BMNP samples have been again verified through the elemental mapping and also observed that the
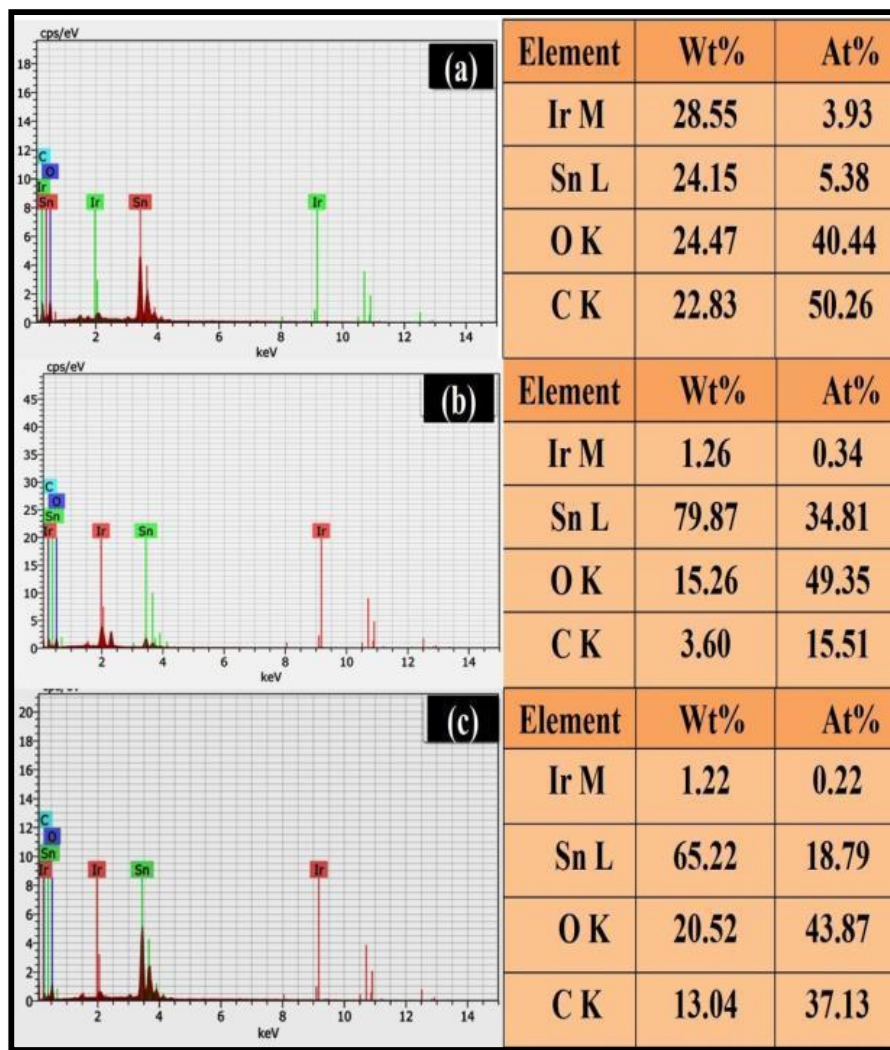
Element	Wt%	At%
Ir M	28.55	3.93
Sn L	24.15	5.38
O K	24.47	40.44
C K	22.83	50.26

Element	Wt%	At%
Ir M	1.26	0.34
Sn L	79.87	34.81
O K	15.26	49.35
C K	3.60	15.51

Element	Wt%	At%
Ir M	1.22	0.22
Sn L	65.22	18.79
O K	20.52	43.87
C K	13.04	37.13

Fig. 7. EDAX spectrum and elemental composition of surfactant assisted BMNP samples (a) Ir-Sn (CTAB) ,(b) Ir-Sn (TSC) and (c)) Ir-Sn (TX-100).

Ir-Sn BNMP elements are uniformly distributed. From the result of EDAX and elemental mapping, it has been observed that the CTAB assisted BMNP nanoparticles are in alloy form and TSC and TX-100 assisted BMNP nanoparticles are in core-shell, and the Ir exist in core and Sn exist in shell, which are exhibited via overlay image in Fig. 8 (d, h, and l). The inset in these images represents the type of bimetallic nanoparticles (alloy and core shell).

Transmission electron microscope (TEM) and High resolution transmission electron microscope (HR-TEM) analysis

The TEM and HRTEM technique have been employed to find the detailed information about the morphology and crystallinity of the surfactant assisted Ir-Sn BMNP samples. The TEM and HR-TEM images of surfactant assisted Ir-Sn BMNP samples reveal that the shapes of crystallite are pseudo spherical (Fig. 9 (a) - (i)). The average diameter of crystallite of the samples have been estimated through the TEM images and it is found to be ~1.39 ± 0.5 nm for Ir-Sn BMNP (CTAB), ~2.2 ± 0.5 nm for Ir-Sn BMNP (TSC), and ~5.79 ± 0.5 nm for Ir-Sn BMNP (TX-100). From the Fig. 9 (a, d, and g), It is clearly seen that the CTAB assisted Ir-Sn BMNP sample are highly dispersed without obvious aggregation as compared to TSC and TX-100 samples. The d-spacing of surfactant assisted Ir-Sn BMNP samples have been evaluated using
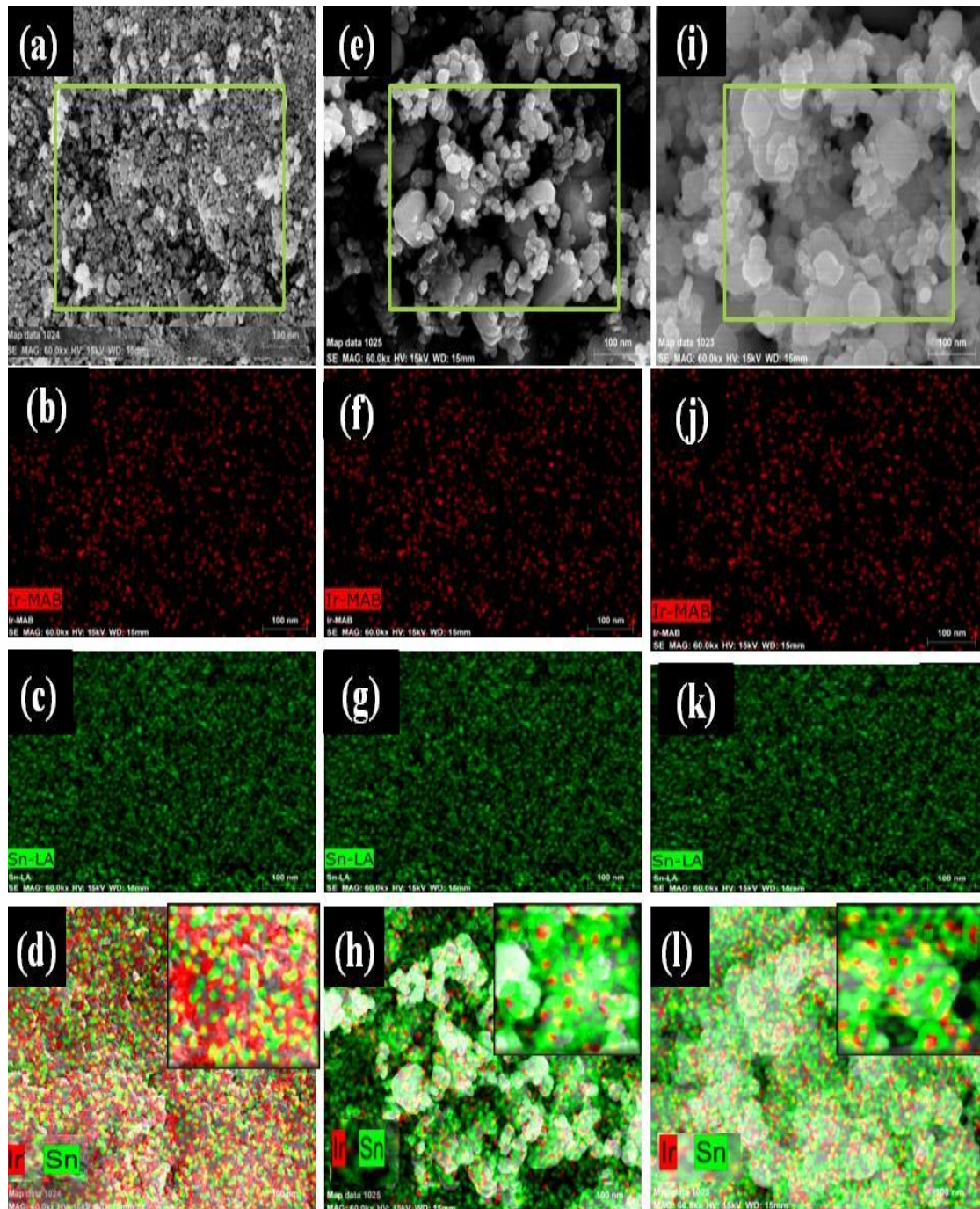
Fig. 8. FE-SEM and corresponding elemental images for surfactant assisted BMNP samples, Ir-Sn : CTAB (a-d), Ir-Sn : TSC (e-h), Ir-Sn :TX-100 (i-l). d, h, l are the overlay images of Ir, Sn. The inset in these images represents the type of bimetallic nanoparticles (alloy and core shell).

the HR-TEM images (Fig. 9 (c), (f), and (i)), and the values of the lattice fringes of d- spacing is 0.285 nm, 0.214 nm and 0.210 nm (CTAB, TSC, and TX-100 assisted samples). These values of

d-spacing are corresponding to (111) crystalline plane of the surfactant assisted Ir-Sn BMNP samples, these (111) plane has the most intense peak in the XRD data of surfactant assisted Ir-Sn
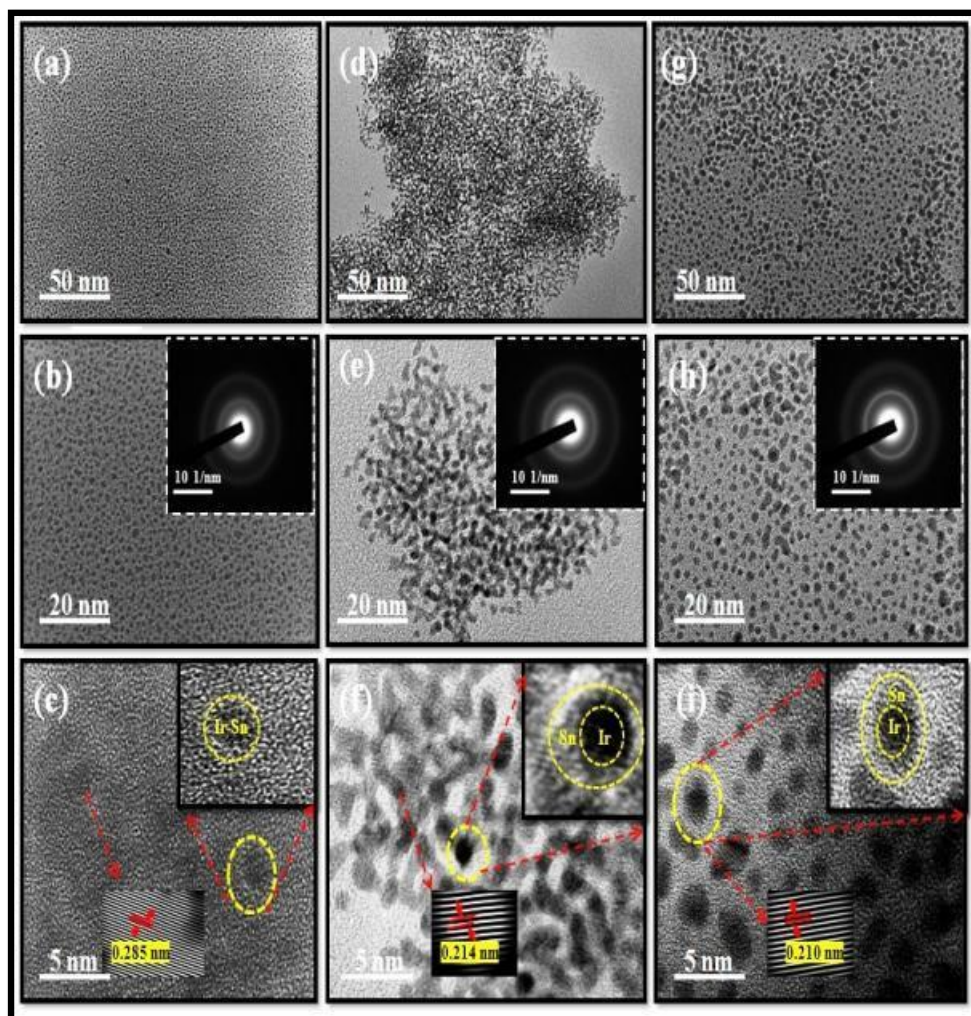
854

Fig. 9. (a)-(i) TEM and HR-TEM image of surfactant assisted Ir-Sn BMNP samples Ir-Sn : CTAB (a-c), Ir-Sn : TSC (d-f), Ir-Sn :TX-100 (g-i) sample, respectively; inset in (b),(e), and (h) presents SAED pattern of samples, (c), (f), and (i) HR-TEM images of samples; inset in the figure depicts the type of bimetallic nanoparticles (alloy and core shell).

BMNP samples (see Fig. 4(d, e, and f). The SAED patterns are recorded from the same region of the images of surfactant assisted Ir-Sn BMNP samples, are shown in the inset of Fig. 9 (b), (e) and (h), respectively. The diffused ring patterns in the SAED images indicate the amorphous nature of the surfactant assisted Ir-Sn BMNP samples, which is in accordance with the XRD result. The inset of Fig. 9 (c), (f), and (i) demonstrate that the surfactant assisted Ir-Sn BMNP samples contain the alloy and core shell like structure. The CTAB assisted Ir-Sn BMNP sample is in alloy form (inset of (c)) and TSC and TX-100 assisted BMNP samples are in core-shell form (inset of (f) and (i)).The inset of Fig. 9 (f) and (i) images also confirm that the Ir

exist in core and Sn exist in shell, which are similar with the FE-SEM elemental mapping results.

X-ray photoelectron spectroscopy (XPS) analysis

X-ray photoemission spectroscopy (XPS) has been carried out to emanate wide information related to the elemental composition and oxidation states of constituting elements in surfactant-assisted Ir-Sn BMNP samples. The XPS survey spectra are shown in Fig. 10 (a), which indicates that Ir, Sn, C, and O elements are present in surfactant-assisted Ir-Sn BMNP samples. In the present study, the data of CTAB assisted Ir-Sn BMNP sample has been exhibited in Fig. 10 (b to d). The high-resolution spectrum
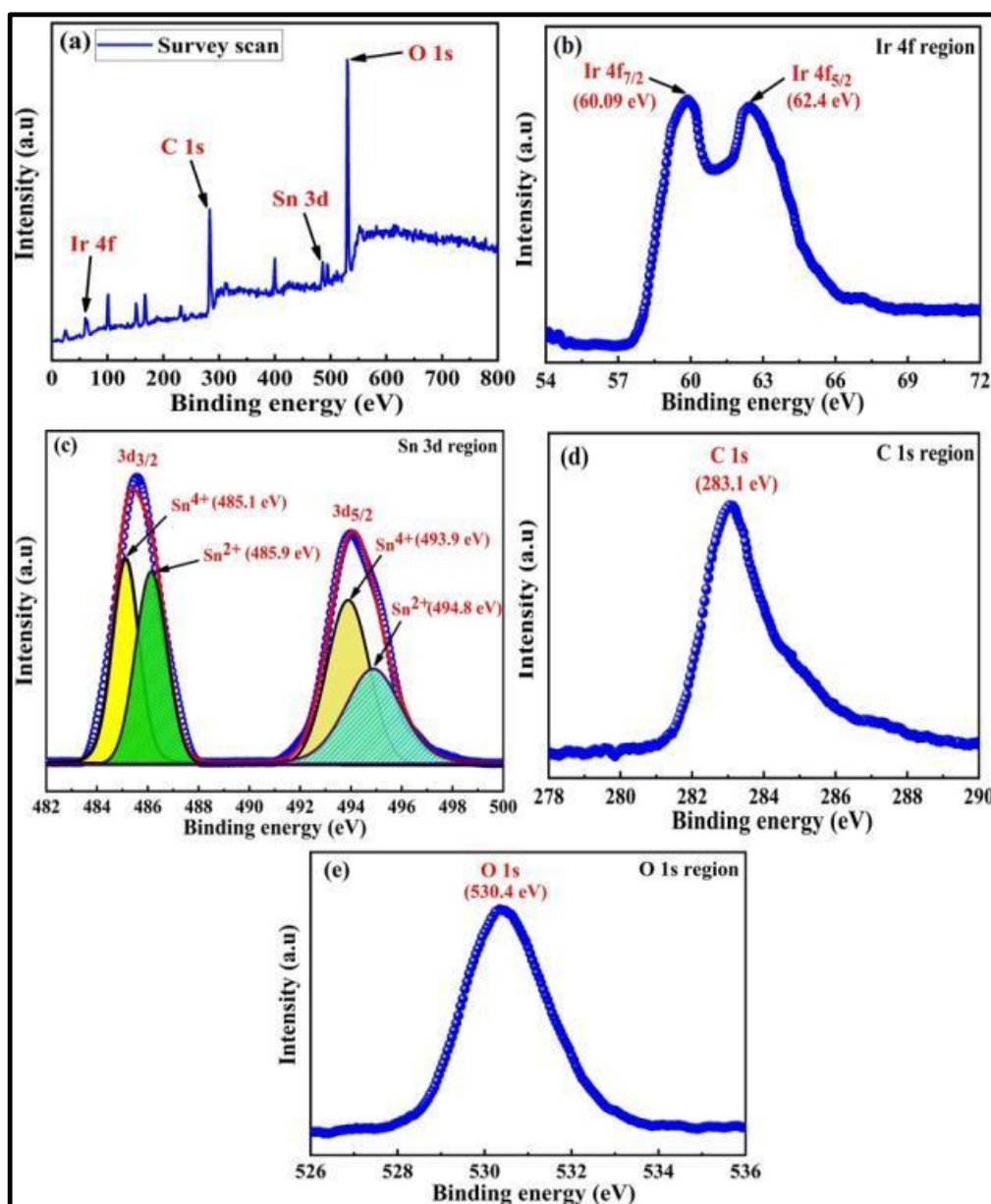
Fig. 10. XPS spectra of CTAB assisted Ir-Sn BMNP sample (a) Survey scan, (b) Ir 4f region, (c) Sn 3d region, (d) C 1s region, and (e) O 1s region.

of Ir 4f region has been demonstrated in Fig. 10 (b). The Ir 4f spectrum reveals that the centered binding energy of Ir $4f_{7/2}$ and Ir $4f_{5/2}$ are 60.09 eV and 62.4 eV respectively, which indicate the formation of metallic iridium (Ir^0) [62-64]. The fitted data of Sn 3d region has been demonstrated in Fig. 10 (c). The Sn 3d spectrum indicates that the binding energy of Sn $3d_{3/2}$ and Sn $3d_{5/2}$ are centered at 485.5 eV and 494.1 eV respectively.

The deconvolution of Sn $3d_{3/2}$ peak into the two peaks at around 485.1 eV and 485.9 eV, while that of the Sn $3d_{5/2}$ peak deconvoluted into two peaks at around 493.9 eV and 494.8 eV confers the best fit to the experimental data [49, 65, 66]. These deconvoluted peaks coincide with two distinct oxidation states of Sn, namely Sn^{4+} and Sn^{2+} (Fig. 10(c)). These deconvolutions of the peaks show the presence of SnO_x in the BMNP samples. SnO
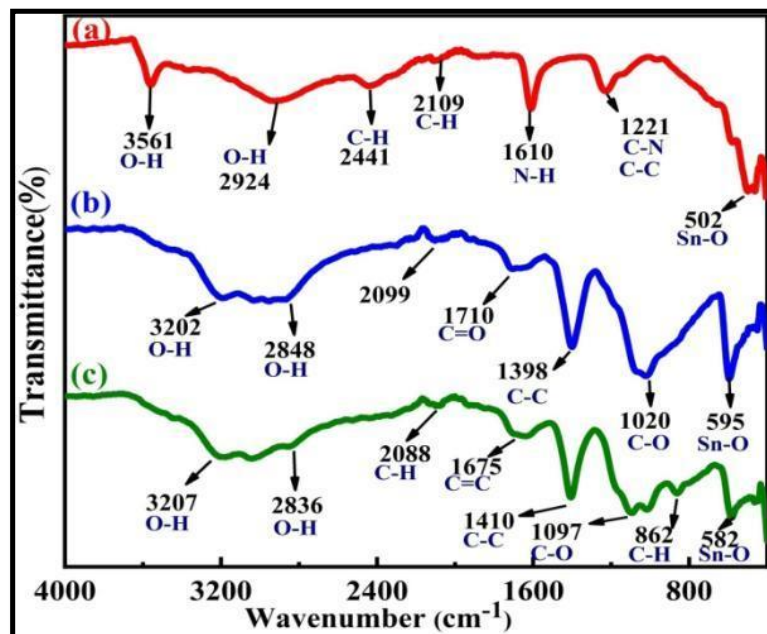
Fig.11. FT-IR spectra of surfactant-assisted BMNP samples (a) Ir-Sn BMNP (CTAB), (b) Ir-Sn BMNP (TSC), and (c) Ir-Sn BMNP (TX-100).

was not detected in the XRD pattern possibly due to SnO content in the sample below the detection limit of XRD. Thus the XPS results also confirm the existence of Sn and incorporation of some amount of Sn into Ir lattice, agreeing with the XRD results. The C 1s spectrum has been exhibited in Fig. 10 (d). The spectrum reveals the binding energy of C 1s is centered at 283.07 eV. This peak stipulated to a carbon atom of a different environment, this may be due to CTAB moiety [51]. The O 1s spectrum has been shown in Fig. 10 (e). The spectrum reveals the binding energy of O 1s is centered at 530.4 eV [62].

Fourier transform infrared spectroscopy (FT-IR) analysis

The presence of the functional groups in the surfactant-assisted Ir-Sn BMNP samples have been examined through the FT-IR spectroscopic analysis, and spectra of all samples are demonstrated in Fig. 11 ((a) Ir-Sn BMNP **(**CTAB), (b) Ir-Sn BMNP (TSC), and **(c)** Ir-Sn BMNP (TX-100)). The FT-IR spectra provide information regarding the local molecular environment of the organic molecules on the surface of the nanoparticles. In spectra of all samples numerous peaks with specific wavenumber are shown, which are related to various functional groups. In Fig. 11(a, b, and c),

the spectra of CTAB, TSC, and TX-100 assisted samples have some peaks around at 3560-3200 cm^{-1} and 2830-2920 cm^{-1}, which may arise due to the O-H stretching vibrations of water molecules [67]. A peak has been observed in all three spectra **(**a, b, c) at different wavenumber values (2109, 2099, and 2088 cm^{-1}), which is developed due to the C-H (aliphatic) stretching vibration. In the same way, a peak has also been observed in CTAB, TSC, and TX-100 assisted samples at different value of wavenumber (1221 cm^{-1}, 1398 cm^{-1}, and 1410 cm^{-1}), that is generated due to the C-C, C-N (aliphatic) stretching vibration. In Fig. 11(c), two peaks have been observed at near about 862 cm^{-1} and 1675 cm^{-1} in the spectra, these are assigned to the C-H (aromatic) stretching and C=C (conjugated) stretching vibrations of the phenyl ring, which is present in the TX-100 assisted sample [68]. In Fig. 11(a), a sharp and strong absorption band has been found at 1610 cm^{-1} in the spectra, which is related to the N-H bending vibration of the amine group that exists in the CTAB assisted sample [55]. Also in Fig. 11 (a) spectra, the weaker band at 2441 cm^{-1} has been seen, which is assigned to the anti-stretching vibration of the C-H group, respectively. In Fig. 11 (b), a band has been observed at 1710 cm^{-1} wavenumber value, which arises due to the C=O stretching of carbonyl group that exists in the

Table 3. Assignment of frequencies of FT-IR spectra of surfactant-assisted Ir-Sn BMNP nanoparticles.

| Assignments of frequencies	(a) Ir-Sn BMNP (CTAB)	(b) Ir-Sn BMNP (TSC)	(c) Ir-Sn BMNP (TX-100)
O-H stretching vibrations	2924 cm^{-1}	2848 cm^{-1}	2836 cm^{-1}
	3561 cm^{-1}	3202 cm^{-1}	3207 cm^{-1}
C=C (aromatic) stretching vibrations	-	-	1675 cm^{-1}
N-H bending vibrations	1610 cm^{-1}	-	-
C-O stretching vibrations	-	1020 cm^{-1}	1097 cm^{-1}
C-C stretching, C-N (aliphatic) vibration	1221 cm^{-1}	1398 cm^{-1}	1410 cm^{-1}
C-H (aliphatic, aromatic) stretching, anti stretching vibration	2109 cm^{-1}	2099 cm^{-1}	2088 cm^{-1}
	2441 cm^{-1}	-	862 cm^{-1}
C=O Stretching vibration	-	1710 cm^{-1}	-
Sn-O-Sn Stretching vibration (metal oxygen bonds)	502 cm^{-1}	595 cm^{-1}	582 cm^{-1}
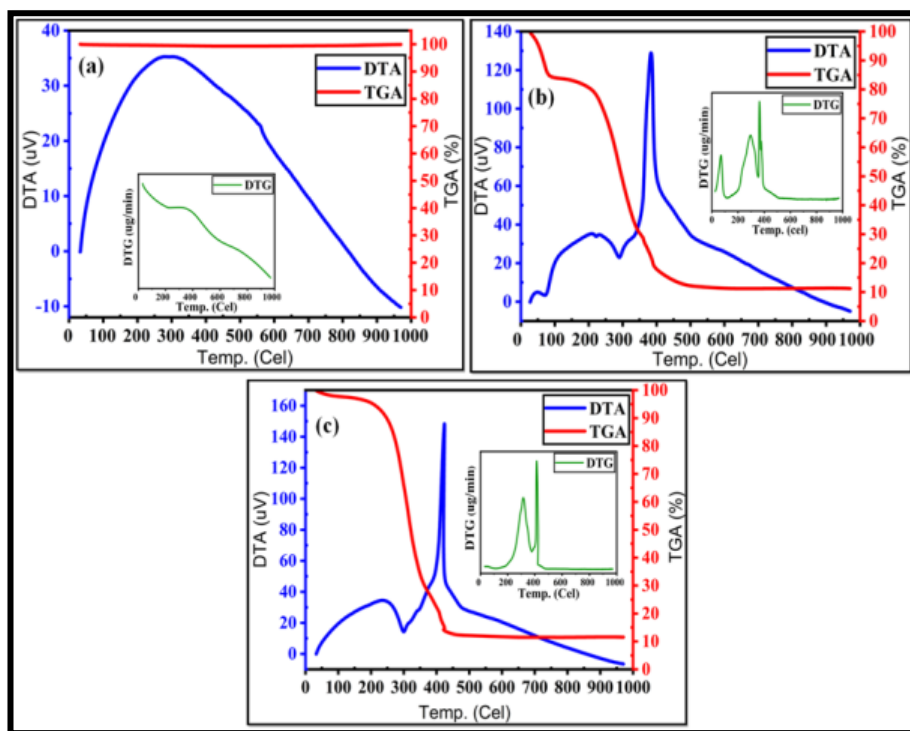
Fig. 12. TGA, DTG and DTA curve of surfactant assisted BMNP samples (a) Ir-Sn BMNP (CTAB) (a) Ir-Sn BMNP (TSC), (c) Ir-Sn BMNP (TX-100), inset in the figure depicts the DTG curve of samples.

TSC assisted sample. The two weak bands have been seen at 1020 cm^{-1} and 1097 cm^{-1} in Fig. 11(b) and Fig. 11(c); these are developed due to the C-O stretching vibration. The strong absorption band observed at 502 cm^{-1}, 595 cm^{-1}, and 582 cm^{-1} wavenumber values, which is related to the Sn-O-Sn (metal oxygen bond) stretching vibration for CTAB, TSC, and TX-100 assisted samples [69]. Hence, the above analysis of the FT-IR spectra of all samples confirms the attachment of the surfactant on the surface of Ir-Sn BMNP samples. The absorption bands that are assigned to the respective vibrations are shown in Table 3.

Thermal analysis (TGA, DTG, and DTA)

The thermal analysis of surfactant-assisted Ir-Sn BMNP samples are examined by employing the TGA, DTG and DTA techniques, and the data of all samples are shown in Fig. 12 (a,b,c). From Fig. 12 (a), the TGA data of Ir-Sn BMNP (CTAB) sample reveals that the sample has a single step of weight loss (~1%) at 100 °C to 400 °C temperature range, the weight loss of the sample is due to the removal of moisture and light volatiles in the sample, but after the 400 °C, the sample shows the weight loss approximately 0.04% up to 900 °C. From the DTG curve (inset of Fig. 12 (a)), the

maximum weight loss of the sample is seen near about 97 °C. In the DTA curve, there is no sharp peak exists in the curve, which indicates that no endothermic and exothermic process occurs in the samples at 35 °C to 1000 °C temperature range. From Fig. 12 (b), the TGA data of the Ir-Sn BMNP (TSC) sample reveals the four steps of degradation of weight. The first step of weight loss is observed amid at 27.2 °C to 84 °C temperature range, which is related to desorption of physically adsorbed water and light volatiles from the surface of nanoparticles with a total loss of about 15.2%. The DTG curve of Ir-Sn BMNP (TSC) shows a sharp peak near about 70 °C, which indicates the maximum weight loss. The second weight loss of the sample occurs in 200 °C to 300 °C temperature range and the total degradation near about 32% of remain sample. The many causes exist of the weight loss of the sample such as the release of the remaining water from the crystalline phase and elimination of the oxygen-based functional groups, which exists on the surface of nanoparticles (i.e., hydroxyl, carboxylic groups) and vanished in the form of gases such as CO_2 and H_2O as a byproduct. The third step of weight loss has been seen amid at 343 °C to 400 °C temperature range. In this range, the weight loss of the remaining sample is approximately 13.7%, which is due to the active pyrolysis and oxidation of the sample. The peaks in the DTG curve (inset of Fig. 12 (b)) verify the maximum change in the weight of the sample near about 287 °C and 389 °C temperature range related to the second and third steps of weight loss. The fourth step of weight loss is observed between 500 °C to 970 °C temperature range, which is approximately equal to 1% of remain sample. The 11.2% weight remains of the sample after all steps occurred. From the DTA curve of Ir-Sn BMNP (TSC) sample, the three peaks have been found at 73 °C, 288 °C, and 384 °C temperature, which is related to the desorption of light volatiles (73 °C) and combustion of any organic residue (288 °C, 384 °C) and these peaks also confirm that the two endothermic and one exothermic process occur in this mechanism. The TGA data of the Ir-Sn BMNP (TX-100) sample, which is shown in Fig. 4(c) reveals the three steps of degradation. In the first step, the weight loss is observed amid 100 °C to 200 °C temperature range, which is occurred due to the removal of physically adsorbed water and light volatiles. The weight loss of the sample in the first step near about 2.2%. In the second

step, the weight loss is approximately 33.5% of the remaining sample, which occurs at 300 °C to 354 °C temperature range, and the reason behind the weight loss is the active pyrolysis and oxidation of the sample. In the third step, the weight loss of the remaining sample is near about 2.4% in the 423°C to 971°C temperature range, which may be due to the degradation of the carbon-carbon skeleton into volatile gases. Only two peaks have been detected in the DTG curve for the Ir-Sn BMNP (TX-100) sample, which are associated with the second or third step degradation and is shown in the inset of Fig.12(c). From the second and third steps, the peaks exist near about at 316 °C and 422 °C, and those are verifying the maximum weight loss of the sample. The remaining weight of the sample after all three steps is almost constant up to 971°C. The DTA curve of the TX-100 assisted sample reveals two peaks at 299 °C and 424 °C temperature; the first peak is at 299 °C temperature, verify the endothermic (minor) process and also confirms the combustion of organic residues. But the second peak, which exists at 424 °C temperature, verify the exothermic (major) process and also confirms the decomposition of some residual absorb species and oxygen at the higher temperature. From the above analysis of TGA, DTG, and DTA curve of surfactant-assisted Ir-Sn BMNP samples, it has been observed that the CTAB assisted sample has better thermal stability as compared to TSC and TX-100 assisted sample.

CONCLUSION

In the present study, we have investigated the effect of surfactant on the particle size and the morphology of Ir-Sn BMNP samples, synthesized via modified polyol method. X-ray diffraction studies verify that the surfactant assisted BMNP samples are amorphous in nature. The minimum crystallite size has been obtained in CTAB assisted Ir-Sn BMNP sample compared to TSC and TX-100 assisted samples, which is evaluated using the XRD data and TEM images. The approximate particle size is assessed by the Image-J software using FE-SEM images, and minimum particle size is found for CTAB assisted sample. The EDAX technique confirms that the Ir, Sn elements are present in Ir-Sn BMNP samples. The EDAX, elemental mapping, and HR-TEM images confirm that the CTAB assisted Ir-Sn BMNP sample is in alloy form and TSC, TX-100 assisted samples are in core-shell form. The results show that CTAB surfactant

plays an important role in controlling the size of particles and stability of Ir-Sn BMNPs sample. The UV-Vis spectroscopy technique is used to monitor the progress of the reaction of the synthesis of nanoparticles. All CTAB, TSC, TX-100 surfactant assisted Ir-Sn BMNP samples exhibited stable new peak around 352 nm in UV-Vis spectra that confirms the formation of bimetallic nanoparticle. The presence of a surfactant in the time of preparation of the nanoparticles not only prompts the nanoparticles to unfold highly active lattice surface, but also prompts the nanoparticles to have the feature of the ordered structure, large surface area, and abundant pores. These variations reform the physico-chemical properties of the nanoparticles, thereby raising the performance of the nanoparticles. The FT-IR technique verifies the interaction between surfactant and Ir-Sn BMNP samples. The thermal analysis reveals that the CTAB assisted Ir-Sn BMNP sample is more stable as compared to TSC and TX-100 assisted samples. The existence of the desired Ir^0 metallic state and Sn dual valence state of Sn 3d core-level is confirmed by XPS spectra.

ACKNOWLEDGEMENTS

CONFLICT OF INTEREST

The authors declare that there is no conflict of interests regarding the publication of this manuscript.

REFERENCES

1. Nasrabadi HT, Abbasi E, Davaran S, Kouhi M, Akbarzadeh A. Bimetallic nanoparticles: Preparation, properties, and biomedical applications. Artificial Cells, Nanomedicine, and Biotechnology. 2014;44(1):376-80.

2. Iyer PV, Ananthanarayan L. Enzyme stability and stabilization—Aqueous and non-aqueous environment. Process Biochemistry. 2008;43(10):1019-32.

3. Joulaei M, Hedayati K, Ghanbari D. Investigation of magnetic, mechanical and flame retardant properties of polymeric nanocomposites: Green synthesis of MgFe2O4 by lime and orange extracts. Composites Part B: Engineering. 2019;176:107345.

4. Boote BW, Byun H, Kim J-H. Silver–Gold Bimetallic Nanoparticles and Their Applications as Optical Materials. Journal of Nanoscience and Nanotechnology. 2014;14(2):1563-77.

5. Song Y, Ma Y, Wang Y, Di J, Tu Y. Electrochemical deposition of gold–platinum alloy nanoparticles on an indium tin oxide electrode and their electrocatalytic applications. Electrochimica Acta. 2010;55(17):4909-14.

6. Fu G, Liu H, You N, Wu J, Sun D, Xu L, et al. Dendritic platinum–copper bimetallic nanoassemblies with tunable composition and structure: Arginine-driven self-assembly and enhanced electrocatalytic activity. Nano Research. 2016;9(3):755-65.

7. Dong Q, Zhao Y, Han X, Wang Y, Liu M, Li Y. Pd/Cu bimetallic nanoparticles supported on graphene nanosheets: Facile synthesis and application as novel electrocatalyst for ethanol oxidation in alkaline media. International Journal of Hydrogen Energy. 2014;39(27):14669-79.

8. Amirsardari Z, Dourani A, Hasanpour F, Amirifar MA, Ghadiri N. Effect of Silica Content on Support-Iridium Active Phase Interactions on the Nanocatalyst Activity. Journal of Nanostructures. 2020;10(2):348-361.

9. Riaz N, Hassan M, Siddique M, Mahmood Q, Farooq U, Sarwar R, et al. Photocatalytic degradation and kinetic modeling of azo dye using bimetallic photocatalysts: effect of synthesis and operational parameters. Environmental Science and Pollution Research. 2019;27(3):2992-3006.

10. Nabiyouni G, Ghanbari D. Simple preparation of magnetic, antibacterial and photo-catalyst NiFe$_2$O$_4$@ TiO$_2$/Pt nanocomposites. Journal of Nanostructures. 2018;8(4):408-416.

11. Eskandari N, Nabiyouni G, Masoumi S, Ghanbari D. Preparation of a new magnetic and photo-catalyst CoFe2O4–SrTiO3 perovskite nanocomposite for photo-degradation of toxic dyes under short time visible irradiation. Composites Part B: Engineering. 2019;176:107343.

12. Krishnan SK, Prokhorov E, Bahena D, Esparza R, Meyyappan M. Chitosan-Covered Pd@Pt Core–Shell Nanocubes for Direct Electron Transfer in Electrochemical Enzymatic Glucose Biosensor. ACS Omega. 2017;2(5):1896-904.

13. Nilekar AU, Alayoglu S, Eichhorn B, Mavrikakis M. Preferential CO Oxidation in Hydrogen: Reactivity of Core–Shell Nanoparticles. Journal of the American Chemical Society. 2010;132(21):7418-28.

14. Li X, Feng J, Perdjon M, Oh R, Zhao W, Huang X, et al. Investigations of supported Au-Pd nanoparticles on synthesized CeO2 with different morphologies and application in solvent-free benzyl alcohol oxidation. Applied Surface Science. 2020;505:144473.

15. Yin Z, Zhou W, Gao Y, Ma D, Kiely CJ, Bao X. Supported Pd–Cu Bimetallic Nanoparticles That Have High Activity for the Electrochemical Oxidation of Methanol. Chemistry – A European Journal. 2012;18(16):4887-93.

16. Che J, Hao M, Yi W, Kobayashi H, Zhou Y, Xiao L, et al. Selective suppression of toluene formation in solvent-free benzyl alcohol oxidation using supported Pd-Ni bimetallic nanoparticles. Chinese Journal of Catalysis. 2017;38(11):1870-9.

17. Xiao K, Bao Z, Qi X, Wang X, Zhong L, Fang K, et al. Structural evolution of CuFe bimetallic nanoparticles for higher alcohol synthesis. Journal of Molecular Catalysis A: Chemical. 2013;378:319-25.

18. Cai S, Duan H, Rong H, Wang D, Li L, He W, et al. Highly Active and Selective Catalysis of Bimetallic Rh3Ni1 Nanoparticles in the Hydrogenation of Nitroarenes. ACS Catalysis. 2013;3(4):608-12.

19. Liu X, Wang D, Li Y. Synthesis and catalytic properties of bimetallic nanomaterials with various architectures. Nano

Today. 2012;7(5):448-66.

20. Sharma G, Kumar A, Sharma S, Naushad M, Prakash Dwivedi R, Alothman ZA, et al. Novel development of nanoparticles to bimetallic nanoparticles and their composites: A review. Journal of King Saud University - Science. 2019;31(2):257-69.

21. Lim J, Yang S, Kim C, Roh C-W, Kwon Y, Kim Y-T, et al. Shaped Ir–Ni bimetallic nanoparticles for minimizing Ir utilization in oxygen evolution reaction. Chemical Communications. 2016;52(32):5641-4.

22. Dietrich C, Uzunidis G, Träutlein Y, Behrens S. Synthesis of Bimetallic Pt/Sn-based Nanoparticles in Ionic Liquids. Journal of Visualized Experiments. 2018(138).

23. Du W, Mackenzie KE, Milano DF, Deskins NA, Su D, Teng X. Palladium–Tin Alloyed Catalysts for the Ethanol Oxidation Reaction in an Alkaline Medium. ACS Catalysis. 2012;2(2):287-97.

24. Frongia F, Pilloni M, Scano A, Ardu A, Cannas C, Musinu A, et al. Synthesis and melting behaviour of Bi, Sn and Sn–Bi nanostructured alloy. Journal of Alloys and Compounds. 2015;623:7-14.

25. Adams RD, Chen M, Elpitiya G, Potter ME, Raja R. Iridium–Bismuth Cluster Complexes Yield Bimetallic Nano-Catalysts for the Direct Oxidation of 3-Picoline to Niacin. ACS Catalysis. 2013;3(12):3106-10.

26. Adams RD, Trufan E. Ruthenium–tin cluster complexes and their applications as bimetallic nanoscale heterogeneous hydrogenation catalysts. Philosophical Transactions of the Royal Society A: Mathematical, Physical and Engineering Sciences. 2010;368(1915):1473-93.

27. Ahn M, Cha IY, Lee JK, Yoo SJ, Sung Y-E. Heterogeneous rhodium–tin nanoparticles: highly active and durable electrocatalysts for the oxidation of ethanol. Journal of Materials Chemistry A. 2015;3(33):17130-4.

28. Elango G, Roopan SM. Efficacy of SnO 2 nanoparticles toward photocatalytic degradation of methylene blue dye. Journal of Photochemistry and Photobiology B: Biology. 2016;155:34-8.

29. Etminan M, Nabiyouni G, Ghanbari D. Preparation of tin ferrite–tin oxide by hydrothermal, precipitation and auto-combustion: photo-catalyst and magnetic nanocomposites for degradation of toxic azo-dyes. Journal of Materials Science: Materials in Electronics. 2017;29(3):1766-76.

30. Cui M-L, Chen Y-S, Xie Q-F, Yang D-P, Han M-Y. Synthesis, properties and applications of noble metal iridium nanomaterials. Coordination Chemistry Reviews. 2019;387:450-62.

31. Goel A, Lasyal R. Iridium nanoparticles with high catalytic activity in degradation of acid red-26: an oxidative approach. Water Science and Technology. 2016;74(11):2551-9.

32. Goel A, Lasyal R. Degradation of Orange G dye by hexacyanoferrate(III) ions in the presence of Iridium nanoparticles: effect of system parameters and kinetic study. Desalination and Water Treatment. 2015;57(37):17547-56.

33. Guo S, Wang E. Noble metal nanomaterials: Controllable synthesis and application in fuel cells and analytical sensors. Nano Today. 2011;6(3):240-64.

34. Goel A, Rani N. Effect of PVP, PVA and POLE surfactants on the size of iridium nanoparticles. Open Journal of Inorganic Chemistry. 2012;02(03):67-73.

35. Kiran V, Ravikumar T, Kalyanasundaram NT, Krishnamurty S, Shukla AK, Sampath S. Electro-Oxidation of Borohydride on Rhodium, Iridium, and Rhodium–Iridium Bimetallic Nanoparticles with Implications to Direct Borohydride Fuel Cells. Journal of The Electrochemical Society. 2010;157(8):B1201.

36. Redel E, Krämer J, Thomann R, Janiak C. Synthesis of Co, Rh and Ir nanoparticles from metal carbonyls in ionic liquids and their use as biphasic liquid–liquid hydrogenation nanocatalysts for cyclohexene. Journal of Organometallic Chemistry. 2009;694(7-8):1069-75.

37. Karan HI, Sasaki K, Kuttiyiel K, Farberow CA, Mavrikakis M, Adzic RR. Catalytic Activity of Platinum Monolayer on Iridium and Rhenium Alloy Nanoparticles for the Oxygen Reduction Reaction. ACS Catalysis. 2012;2(5):817-24.

38. Anjali G. A kinetic and mechanistic study on the oxidation of arginine and lysine by hexacyanoferrate (III) catalysed by iridium (III) in aqueous alkaline medium. Journal of Chemical Engineering and Materials Science. 2012;3(1).

39. Pi Y, Shao Q, Zhu X, Huang X. Dynamic structure evolution of composition segregated iridium-nickel rhombic dodecahedra toward efficient oxygen evolution electrocatalysis. ACS nano. 2018;12(7):7371-7379.

40. Du W, Deskins NA, Su D, Teng X. Iridium–Ruthenium Alloyed Nanoparticles for the Ethanol Oxidation Fuel Cell Reactions. ACS Catalysis. 2012;2(6):1226-31.

41. Xu J, Lian Z, Wei B, Li Y, Bondarchuk O, Zhang N, et al. Strong Electronic Coupling between Ultrafine Iridium–Ruthenium Nanoclusters and Conductive, Acid-Stable Tellurium Nanoparticle Support for Efficient and Durable Oxygen Evolution in Acidic and Neutral Media. ACS Catalysis. 2020;10(6):3571-3579.

42. Zhang R, Chen W. Non-precious Ir–V bimetallic nanoclusters assembled on reduced graphene nanosheets as catalysts for the oxygen reduction reaction. Journal of Materials Chemistry A. 2013;1(37):11457.

43. Chang S-H, Yeh M-H, Rick J, Su W-N, Liu D-G, Lee J-F, et al. Bimetallic catalyst of PtIr nanoparticles with high electrocatalytic ability for hydrogen peroxide oxidation. Sensors and Actuators B: Chemical. 2014;190:55-60.

44. Courtois J, Du W, Wong E, Teng X, Deskins NA. Screening iridium-based bimetallic alloys as catalysts for direct ethanol fuel cells. Applied Catalysis A: General. 2014;483:85-96.

45. Xu R, Lian K, Xu Z, Yue Y, Yuan P, Bao X, et al. Controllable synthesis of Ir(Rh)–Sn/SiO2 bimetallic catalysts via surface organometallic chemistry for the production of ethanol from hydrogenolysis of ethyl acetate. Catalysis Science & Technology. 2020;10(4):1086-95.

46. Liang Q, Liu X, Zeng G, Liu Z, Tang L, Shao B, et al. Surfactant-assisted synthesis of photocatalysts: Mechanism, synthesis, recent advances and environmental application. Chemical Engineering Journal. 2019;372:429-51.

47. Guo P, Chen P, Liu M. One-Dimensional Porphyrin Nanoassemblies Assisted via Graphene Oxide: Sheetlike Functional Surfactant and Enhanced Photocatalytic Behaviors. ACS Applied Materials & Interfaces. 2013;5(11):5336-45.

48. Ma C-l, Sun X-d. Preparation and characterization of SnO_2 nanoparticles with a surfactant-mediated method. Nanotechnology. 2002;13(5):565.

49. Haspulat B, Sarıbel M, Kamış H. Surfactant assisted hydrothermal synthesis of SnO nanoparticles with enhanced photocatalytic activity. Arabian Journal of Chemistry. 2020;13(1):96-108.

50. Fiévet F, Ammar-Merah S, Brayner R, Chau F, Giraud M, Mammeri F, et al. The polyol process: a unique method

for easy access to metal nanoparticles with tailored sizes, shapes and compositions. Chemical Society Reviews. 2018;47(14):5187-233.

51. Goel A, Chaudhary M. Highly dispersed PVP-supported Ir–Ni bimetallic nanoparticles as high performance catalyst for degradation of metanil yellow. Bulletin of Materials Science. 2018;41(3).

52. Xu D, Diao P, Jin T, Wu Q, Liu X, Guo X, et al. Iridium Oxide Nanoparticles and Iridium/Iridium Oxide Nanocomposites: Photochemical Fabrication and Application in Catalytic Reduction of 4-Nitrophenol. ACS Applied Materials & Interfaces. 2015;7(30):16738-49.

53. Rac O, Suchorska-Woźniak P, Fiedot M, Teterycz H. Influence of stabilising agents and pH on the size of SnO2 nanoparticles. Beilstein Journal of Nanotechnology. 2014;5:2192-201.

54. Bakshi MS. How Surfactants Control Crystal Growth of Nanomaterials. Crystal Growth & Design. 2015;16(2):1104-33.

55. Sujatha K, Seethalakshmi T, Sudha AP, Shanmugasundaram OL. Photocatalytic activity of pure, Zn doped and surfactants assisted Zn doped SnO2 nanoparticles for degradation of cationic dye. Nano-Structures & Nano-Objects. 2019;18:100305.

56. Gnanam S, Rajendran V. Anionic, cationic and nonionic surfactants-assisted hydrothermal synthesis of tin oxide nanoparticles and their photoluminescence property. Digest Journal of Nanomaterials and Biostructures. 2010;5(2):623.

57. Basnet P, Chatterjee S. Structure-directing property and growth mechanism induced by capping agents in nanostructured ZnO during hydrothermal synthesis—A systematic review. Nano-Structures & Nano-Objects. 2020;22:100426.

58. Abràmoff MD, Magalhães PJ, Ram SJ. Image processing with ImageJ. Biophotonics international. 2004;11(7):36-42.

59. Raghav DS, Kumari S, Singh HK, Varma GD. Structure, magnetism and electrical transport of sol-gel derived La0.30Pr0.30Ca0.40MnO3: Elucidating consequences of size effect. Journal of Magnetism and Magnetic Materials. 2020;497:166003.

60. Dhamodharan P, Gobi R, Shanmugam N, Kannadasan N, Poonguzhali R, Ramya S. Synthesis and characterization of surfactants assisted Cu2+ doped ZnO nanocrystals.

Spectrochimica Acta Part A: Molecular and Biomolecular Spectroscopy. 2014;131:125-31.

61. Liang Q, Liu X, Zeng G, Liu Z, Tang L, Shao B, et al. Surfactant-assisted synthesis of photocatalysts: Mechanism, synthesis, recent advances and environmental application. Chemical Engineering Journal. 2019;372:429-51.

62. Dhanalakshmi M, Saravanakumar K, Lakshmi Prabavathi S, Abinaya M, Muthuraj V. Fabrication of novel surface plasmon resonance induced visible light driven iridium decorated SnO2 nanorods for degradation of organic contaminants. Journal of Alloys and Compounds. 2018;763:512-24.

63. Kumar S, Chinnathambi S, Munichandraiah N. Ir nanoparticles-anchored reduced graphene oxide as a catalyst for oxygen electrode in Li–O2 cells. New Journal of Chemistry. 2015;39(9):7066-75.

64. Tamura M, Tokonami K, Nakagawa Y, Tomishige K. Effective NbOx-Modified Ir/SiO2 Catalyst for Selective Gas-Phase Hydrogenation of Crotonaldehyde to Crotyl Alcohol. ACS Sustainable Chemistry & Engineering. 2017;5(5):3685-97.

65. Kumar M, Bhatt V, Abhyankar AC, Kim J, Kumar A, Patil SH, et al. New insights towards strikingly improved room temperature ethanol sensing properties of p-type Ce-doped SnO2 sensors. Scientific Reports. 2018;8(1).

66. Liu J, Wang C, Yang Q, Gao Y, Zhou X, Liang X, et al. Hydrothermal synthesis and gas-sensing properties of flower-like Sn3O4. Sensors and Actuators B: Chemical. 2016;224:128-33.

67. Moradi B, Nabiyouni G, Ghanbari D. Rapid photo-degradation of toxic dye pollutants: green synthesis of mono-disperse Fe3O4–CeO2 nanocomposites in the presence of lemon extract. Journal of Materials Science: Materials in Electronics. 2018;29(13):11065-80.

68. Hubetska TS, Krivtsov I, Kobylinska NG, Garcia Menendez JR. Hydrophobically Functionalized Magnetic Nanocomposite as a New Adsorbent for Preconcentration of Organochlorine Pesticides in Water Solution. IEEE Magnetics Letters. 2018;9:1-5.

69. Kiani A, Nabiyouni G, Masoumi S, Ghanbari D. A novel magnetic MgFe2O4–MgTiO3 perovskite nanocomposite: Rapid photo-degradation of toxic dyes under visible irradiation. Composites Part B: Engineering. 2019;175:107080.